Optoelectronic and mechanical properties of the orthogonal and tetragonal Cu$_2$CdGe(S$_x$Se$_{1-x}$)$_4$ semiconducting system via first principles methods ⓔⓟ

V. T. Barone, ⓘ B. B. Dumre, ⓘ B. R. Tuttle, et al.

COLLECTIONS

ⓔⓟ   This paper was selected as an Editor's Pick

View Online   Export Citation   CrossMark

ARTICLES YOU MAY BE INTERESTED IN

Substrate-dependence of monolayer MoS$_2$ thermal conductivity and thermal boundary conductance
Journal of Applied Physics **131**, 195103 (2022); https://doi.org/10.1063/5.0089247

Phonon transport in the gigahertz to terahertz range: Confinement, topology, and second sound
Journal of Applied Physics **131**, 180901 (2022); https://doi.org/10.1063/5.0073508

Enhancing one-dimensional particle-in-cell simulations to self-consistently resolve instability-induced electron transport in Hall thrusters
Journal of Applied Physics **131**, 193302 (2022); https://doi.org/10.1063/5.0090853

Optoelectronic and mechanical properties of the orthogonal and tetragonal $Cu_2CdGe(S_xSe_{1−x})_4$ semiconducting system via first principles methods (EP)

View Online   Export Citation   CrossMark

V. T. Barone,[1] B. B. Dumre,[1] (iD) B. R. Tuttle,[2] (iD) and S. V. Khare[1,a] (iD)

AFFILIATIONS

[1]Department of Physics and Astronomy, Wright Center for Photovoltaics Innovation and Commercialization (PVIC),
University of Toledo, Toledo, Ohio 43606, USA
[2]Department of Physics, Penn State Behrend, Erie, Pennsylvania 16563, USA

[a]Author to whom correspondence should be addressed: sanjay.khare@utoledo.edu

ABSTRACT

We computationally investigate the tetragonal and orthorhombic $Cu_2CdGe(S_xSe_{1−x})_4$ ($0 \leq x \leq 1$) alloy systems and study their mechanical and optoelectronic properties for photovoltaic applications using first principles density functional theory and beyond methods. Formation energies are all below $−5.5$ eV/f.u., decreasing with x. Energy vs strain calculations estimate the bulk moduli to be between 55 and 69 GPa, the shear moduli to be between 22 and 28 GPa, and Young's moduli to be between 59 and 74 GPa, all monotonically increasing with x. Optoelectronic properties are computed with the hybrid HSE06 functional. Bandgaps between 1.2 and 1.9 eV (increasing with x), low carrier masses in the (001) direction, and favorable optical absorption and reflectivity indicate that the alloys could be used as an absorber layer in solar cells. For a given value of x, the tetragonal system has higher elastic constants, a lower bandgap, and lower effective masses for both electrons and holes compared to the orthorhombic system. Further, the absorption coefficient near the peak of the standard AM 1.5 solar spectrum is calculated to be $5\,\mu m^{−1}$ larger for the tetragonal system than for the orthorhombic system. These considerations lead to the conclusion that the tetragonal system shows promise as an absorber material for both single-junction and tandem solar cells.

I. INTRODUCTION

The increasing demand for renewable energy devices has previously led to $Cu(In, Ga)Se_2$ and CdTe being projected as the dominant thin-film absorber materials for photovoltaic (PV) applications on account of their competitive power conversion efficiency (PCE) values and low cost compared to crystalline silicon solar cells. Since In and Ga are rare, hence expensive and Cd is toxic, more recent interest has been focused on Cu_2-XII-XIV-XVI_4 materials excluding In and Ga. Of these materials, $Cu_2ZnSn(S, Se)_4$ has attracted the most attention[1–6] with Wang *et al.*[1] creating a device achieving 12.6% PCE. Other materials in the same family have also been used/considered for PV, biosensing, and thermoelectric applications.[7–17] Despite holding the record PCEs for Cu_2-XII-XIV-XVI_4 devices, there are indications that $Cu_2ZnSn(S, Se)_4$ is not the best choice of the quaternary copper chalcogenides for PV applications. Issues with band tailing and bulk defects continue to limit the open circuit voltage and bottleneck the PCE of devices based on the material.[18,19]

$Cu_2CdGe(XVI)_4$ (XVI = S, Se) is a related system with promise for PV applications. Notably, the work of Grossberg *et al.*[20] on the optical properties of $Cu_2CdGeSe_4$ has suggested that this material may be able to overcome PCE-limiting factors present in Cu_2ZnSn $(S, Se)_4$.[21] $Cu_2CdGeSe_4$ has a bandgap between 1.14 and 1.27 eV depending on its growth conditions.[10,22,23] Gulay *et al.* and Marushko *et al.*[24,25] describe that depending on the synthetization temperature, $Cu_2CdGeSe_4$ grows with either tetragonal or orthorhombic symmetry. Cu_2CdGeS_4, on the other hand, always has orthorhombic symmetry.[25] $Cu_2CdGeSe_4$ has also been considered for PV applications and has a relatively high bandgap of around 2.0 eV.[22,26,27]

For PV applications, a benefit of $Cu_2CdGeSe_4$ is the potential for anion substitution with S, as recently described by an experimental study of Li et al.[22] They explored the $Cu_2CdGe(S_xSe_{1-x})_4$ system and tuned the bandgap from 1.27 to 2.04 eV, creating a device with a PCE of 6.4%. Li et al. focused on the orthorhombic (o-) $Cu_2CdGe(S_xSe_{1-x})_4$ system, leaving tetragonal (t-) phase $Cu_2CdGe(S_xSe_{1-x})_4$ mostly unexplored. This may be due to the difficulty of growing the mixed-phase t-$Cu_2CdGe(S_xSe_{1-x})_4$.

Given the recent experimental interest in the $Cu_2CdGe(S_xSe_{1-x})_4$ system, there is a need for a theoretical examination of its physical and electrical properties. First principles modeling has previously been used to elucidate the properties of similar alloy systems.[28–35] With this in mind, the present study uses first principles calculations to explore both the t- and o-phases of $Cu_2CdGe(S_xSe_{1-x})_4$, using advanced HSE06 functionals to properly capture their optoelectronic characteristics. We vary $x = [S]/([S] + [Se])$ such that $0 \leq x \leq 1$ in steps of $\Delta x = 0.125$.

The paper is organized as follows: first, we detail our computational methods in Sec. II. Then, we characterize structural properties and elastic properties in Sec. III A, followed by a discussion of the optoelectronic properties of the system in Sec. III B. Finally, in Sec. IV, we conclude by reviewing the potential of $Cu_2CdGe(S_xSe_{1-x})_4$ for PV applications and list ideas for future research.

II. COMPUTATIONAL METHODS

All computations were performed with the plane wave Vienna Ab Initio Simulation Package (VASP).[36,37] The plane wave cutoff energy was fixed at 550 eV.[38] For structural relaxations, we treat exchange-correlation effects with the Perdew–Burke–Ernzerhof (PBE) functional[39] and employ standard projector-augmented wave potentials[40] to describe the core electrons. The following pseudopotential basis sets were utilized: Cu, Cd, Ge, Se, and S. Γ-centered k-point meshes of size ($8 \times 8 \times 7$) were generated according to the Monkhorst–Pack scheme.[41] For relaxations, Gaussian smearing with width $(\sigma) = 0.04$ eV was used to set partial occupancies of electrons.[42,43] Cell size, shape, and atomic positions were optimized until the forces on each atom were less than 1 meV/Å.[34] The criterion for electronic convergence was set to when the change in energy was less than 10^{-7} eV.

To model $Cu_2CdGe(S_xSe_{1-x})_4$, we use established structures for end members from the Materials Project[44] as starting points. First reported by Gulay et al.,[24] t-$Cu_2CdGeSe_4$ takes the stannite structure, with the following (element, Wyckoff position) pairs: (Cu, 4d), (Cd, 2a), (Ge, 2b), and (Se, 8i). Alternatively, o-$Cu_2CdGeSe_4$ takes the wurtzite structure with the following (element, Wyckoff position) pairs: (Cu, 2a), (Ge, 2a), (Se2 & Se3, 2a), (Se1, 4b), and (1/2 Cu + 1/2 Cd, 4b). The starting model used in this work is that of Materials Project ID mp-13982. We then linearly interpolated lattice vector lengths between one end member and the other. The x condition for each of the seven intermediate structures for both t- and o-$Cu_2CdGe(S_xSe_{1-x})_4$ was fulfilled by randomly filling the anionic sites with either S or Se. These starting structures were then allowed to fully relax all atomic positions, cell shapes, and volumes according to the quantitative parameters described above. We calculated lattice parameters and the bandgap at the GGA level for different representations of the same x to

ensure that basic properties were independent of which S sites were changed to Se. Specifically, we tested three representations of each x (out of a possible $\binom{8}{8x}$ combinations). The maximum deviations from the average lattice constant, cell angle, and bandgap were 0.04 Å, 0.3°, and 0.04 eV, respectively. Thus, we consider these parameters constant to about 0.1 Å, 1°, and 0.1 eV and expect that other reported values are constant as well. To further analyze the structures, we used the Visualization for Electronic and Structural Analysis software (VESTA, version 3.4.5[45])to simulate powder diffraction patterns.

Formation energies were calculated with respect to bulk materials using standard methods.[46,47] Models for all bulk materials were taken from Materials Project[44] and have the following IDs: Cu: mp-30, Cd: mp-1096861, Ge: mp-32, Se: mp-14, and S: mp-994911. Specifically, we used the formula

$$E_{form}(x) = E_{CCG(Se, S)}(x) - 2E_{Cu} + E_{Cd} + E_{Ge} + 4[E_S x + E_{Se}(1 - x)],$$

where E_{form} is the formation energy per formula unit, $E_{CCG(Se, S)}$ is the energy of $Cu_2CdGe(S_xSe_{1-x})_4$ for a given x, and E_i is the energy per atom of the ith element in its bulk configuration.

To explore charge transfer as a function of [S], we computed the effective charges for each element using Bader analysis as implemented in the Henkelman Group's Bader Analysis code.[48–51] Bader's charge analysis is based only on the density and interfaces directly with VASP and is, thus, a natural choice in comparison to other charge analysis methods, such as Mulliken (based on LCAO) or Hirshfeld (which must be parameterized). For the charge analysis, we increased the density of the FFT grid from the default by a factor of 3.5.[52]

To calculate elastic properties, we employed the energy-strain method,[53–55] using deformation matrices described in Ravindran et al.[56] (except for the center entry of D_9, which we changed to $1 + \delta/(1 - \delta^2)^{1/3}$ in order to better conserve the cell volume) with strain parameter δ ranging from -0.002 to $+0.002$ in steps of 0.001. The relatively small choice of δ allowed for faster convergence of elastic constant calculations, permissible due to the strict force tolerances and electronic convergence criteria used. Elastic properties (bulk, shear, Young's moduli, Vickers hardness, and the Debye temperature) were calculated according to appropriate equations in Refs. 42, 57, and 58. The directional dependence of Young's modulus was calculated according to Eq. (7) in Chen et al.,[59] and the structural stability of all models was evaluated using the following Born stability criteria (originally given by Mouhat et al.[60]):

$$\begin{cases} C_{ii} > 0 \ for \ i \in \{1, \ 4, \ 5, \ 6\}, \\ C_{11}C_{22} - C_{12}^2 > 0, \\ C_{11}C_{22}C_{33} + 2C_{12}C_{13}C_{23} - C_{11}C_{23}^2 - C_{22}C_{13}^2 - C_{33}C_{12}^2 > 0. \end{cases}$$

To study the dynamical stability of $Cu_2CdGe(S_xSe_{1-x})_4$, we employ the Phonopy software package,[61] which calculates the force constant matrix of a structure through the frozen phonon method. For these calculations, we extend both the tetragonal and

orthorhombic cells into $2 \times 2 \times 2$ supercells. Each structure's stability is determined by the presence of any imaginary phonon frequencies—if any imaginary phonon frequencies exist, that structure is dynamically unstable.

For optoelectronic properties, we used the Heyd–Scuseria–Ernzerhof hybrid functional[62] (HSE06) since its prediction of the bandgap is known to agree with the experiment much better than local density and generalized gradient methods.[63–65] Convergence tests and previous studies showed that reducing the k-point mesh to $(6 \times 6 \times 5)$ gave acceptable results with HSE06.[66,67] We used the tetrahedron method with Blöchl corrections[68] to set partial occupancies of electrons.[69,70]

The Crystal Orbital Hamilton Population (COHP) analysis was carried out using the Local Orbital Basis Suite Towards Electronic-Structure Reconstruction (LOBSTER, version 4.0.0[71–76]) program using the following default basis functions: Cu: 3d + 4s, Cd: 4d + 5s, Ge: 4p + 4s, Se: 4p + 4s, S: 3p + 3s. This resulted in a charge spilling of $\leq 1.3\%$. We considered all atom pairs between 1 and 3.2 Å for these calculations. The COHP, similar to the Crystal Orbital Overlap Population (COOP) analysis, can indicate relative bond strength. We choose to use the COHP over COOP due to COHP's partitioning of band structure energies instead of COOP's partitioning of electrons into bonding contributions (the former is better suited to density functional theory).

We have calculated carrier effective masses (m^*) using the scheme originally suggested by Hautier et al.[77] that considers the energy landscape of the entire Brillouin zone and allows for tunable temperatures and chemical potentials. The (ith, jth) component of the inverse of the averaged effective mass tensor M_{ij}^{-1} is given by

$$\left\langle M_{ij}^{-1} \right\rangle = -\left(\sum_{b=\text{bands}} \int \frac{d^3\mathbf{k}}{(2\pi)^3} \frac{1}{\hbar^2} \frac{\partial^2 E_b(\mathbf{k})}{\partial k_i \partial k_j} n_{\text{FD}}(\mathbf{k}) \right) \times \left(\sum_{b=\text{bands}} \int \frac{d^3\mathbf{k}}{(2\pi)^3} n_{\text{FD}}(\mathbf{k}) \right)^{-1},$$

where $E_b(\mathbf{k})$ is the energy of the bth band at point $\mathbf{k}$ and n_{FD} is the Fermi–Dirac distribution with chemical potential μ at temperature T,

$$n_{\text{FD}}(\mathbf{k}) = \left(\exp\left[\pm \frac{E_b(\mathbf{k}) - \mu}{kT} \right] + 1 \right)^{-1}.$$

We choose $T = 300\,\text{K}$ and μ to lie just above (below) the valance (conduction) band edge. From the mass tensor, we report the so-called "conductivity mass," which is the harmonic average of its eigenvalues. The consistent choices of T and μ allow for effective comparisons between structures and concentrations of [S], while the non-zero T allows for the inclusion of nonparabolicity and multiple extrema in the energy landscape to the effective mass.

Finally, the optical response functions were calculated within VASP according to independent particle approximation (IPA) outlined in Gajdoš et al.[78] Specifically, using the notation of Ref. 79, the (ith, jth) component of the frequency (ω)-dependent imaginary dielectric tensor is calculated as

$$\varepsilon_{2ij} = \frac{4\pi^2 e^2}{V} \lim_{q \to 0} \left[\frac{1}{q^2} \sum_{c,v,\mathbf{k}} 2\omega_k \delta(\varepsilon_{c\mathbf{k}} - \varepsilon_{v\mathbf{k}} - \omega) \times \left\langle u_{c\mathbf{k}+\mathbf{e}_i q} \mid u_{v\mathbf{k}} \right\rangle \left\langle u_{v\mathbf{k}} \mid u_{c\mathbf{k}+\mathbf{e}_j q} \right\rangle \right],$$

where the sum is over conduction bands c, valance bands v, and k-points $\mathbf{k}$. u represents the periodic cell portion of the orbitals. The real part of the dielectric tensor is given by

$$\varepsilon_{1ij} = 1 + \frac{2}{\pi} \int_0^\infty \frac{\varepsilon_{2ij}(\omega')\omega'}{\omega'^2 - \omega^2 + i\eta} \, d\omega',$$

where the integral is a principal value integral and η is a small complex shift (chosen as the VASP default, $\eta = 0.1$). In order to ensure that enough empty conduction band states were included for convergence, we increased the number of calculated bands from the default by a factor of 3.[79] The IPA paired with the HSE06 functional is a reasonable compromise between accuracy and computational efficiency—resource limitations made using more advanced theories (induced dipole, GW, Bethe Salpeter, and Casida equations) intractable.

III. RESULTS

A. Structural and elastic properties

1. Lattice parameters

Our calculated lattice parameters, formation energies (E_{form}), and free energies (F) of the Cu$_2$CdGe(S$_x$Se$_{1-x}$)$_4$ system are tabulated in Table I. The lattice lengths of t-Cu$_2$CdGeSe$_4$, o-Cu$_2$CdGeSe$_4$, and o-Cu$_2$CdGeS$_4$ match well with the previous experimental results obtained through x-ray powder diffraction (XRD) analysis[10,20,22–24,26,27] and theoretical DFT calculations.[28,31–33] As for intermediate phases, the lattice parameters are roughly linear in x, in agreement with the experimental observations of Li et al. via XRD.[22] The c/a ratio (=1.9) of t-Cu$_2$CdGe(S$_x$Se$_{1-x}$)$_4$ remains constant over all x. It is also in between the c/a ratios for similar tetragonal materials, such as Cu$_2$-XII-XIV-XVI$_4$ (XII = Cd, Zn, XIV = Si, Ge, Sn, XVI = S, Se, Te), for which XRD analysis has given values between 1.8 and 2.0.[7–11,13–16] Not only are both o-Cu$_2$CdGe(S$_x$Se$_{1-x}$)$_4$'s c/a ratio (=1.2) and b/a ratio (=1.0) constant, but they also match experimental values (obtained

TABLE I. Structural parameters for tetragonal (t-) and orthorhombic (o-) $Cu_2CdGe(S_xSe_{1-x})_4$ phases including lattice vector lengths (a, b, c) in Å, formation energies (E_{form}) in eV/f.u., and Helmholtz free energies at 300 K (F) in kJ/mol. Cell angles are all equal to 90° to within ± 0.4°.

	t-$Cu_2CdGe(S_xSe_{1-x})_4$				o-$Cu_2CdGe(S_xSe_{1-x})_4$				
x	a	c	E_{form}	F	a	b	c	E_{form}	F
0.000	5.9, (5.8)[a,b,f,g], (5.6)[h]	11.3, (11.1)[a,b,f,g], (10.7)[h]	−5.6	−33.6	6.7, (6.6)[a,b,c]	7.0, (6.9)[a,b,c]	8.2, (8.1)[a,b,c]	−5.5	−34.5
0.125	5.8, (5.7)[e]	11.2, (11.0)[e]	−5.7	−32.0	6.6, (6.6)[e]	7.0, (6.8)[e]	8.2, (8.0)[e]	−5.7	−31.6
0.250	5.8	11.1	−5.9	−29.9	6.6, (6.5)[e]	6.9, (6.8)[e]	8.1, (8.0)[e]	−5.9	−29.6
0.375	5.7	11.0	−6.1	−27.6	6.6, (6.5)[e]	6.9, (6.8)[e]	8.0, (7.9)[e]	−6.0	−27.5
0.500	5.7	10.9	−6.2	−24.6	6.5, (6.5)[e]	6.8, (6.7)[e]	8.0, (7.9)[e]	−6.2	−25.0
0.625	5.7	10.9	−6.4	−22.8	6.5, (6.4)[e]	6.8, (6.8)[e]	7.9, (7.8)[e]	−6.4	−22.8
0.750	5.6	10.8	−6.6	−20.5	6.4, (6.4)[e]	6.7, (6.7)[e]	7.9, (7.8)[e]	−6.6	−19.9
0.875	5.6	10.7	−6.9	−17.5	6.4, (6.3)[e]	6.7, (6.6)[e]	7.8, (7.8)[e]	−6.8	−17.4
1.000	5.6, (5.5)[g]	10.6, (10.6)[g]	−7.1	−16.0	6.4, (6.3)[d,c,b], (6.4)[i]	6.6, (6.6)[d,c,b,i]	7.8, (7.7)[d,c,b], (7.8)[i]	−7.1	−14.4

[a]References 20, 24, and 26 (experimental).
[b]Reference 22 (experimental).
[c]Reference 10 (experimental).
[d]References 26 and 27 (experimental).
[e]Linear interpolations (the step size of Li *et al.*[22] was $\Delta x = 0.2$, while ours was $\Delta x = 0.125$).
[f]Reference 32 (theoretical).
[g]Reference 33 (theoretical).
[h]Reference 28 (theoretical).
[i]Reference 31 (theoretical).

through XRD) of Cu_2-XII-XIV-XVI_4 (XII = Cd, Zn, XIV = Si, Ge, XVI = S, Se).[8,9,15] The constant lattice parameters indicate that the general shape of the alloy is conserved while the size changes with x.

The formation energies (E_{form}) follow a linear trend in x, with Cu_2CdGeS_4 being about 1.5 eV lower in energy than $Cu_2CdGeSe_4$. t-$Cu_2CdGe(S_xSe_{1-x})_4$ is lower in energy than o-$Cu_2CdGe(S_xSe_{1-x})_4$ for any given x, which is consistent with the experimental observation that o-$Cu_2CdGe(S_xSe_{1-x})_4$ must be synthesized in an environment around 200 K higher in temperature than t-$Cu_2CdGe(S_xSe_{1-x})_4$, which is grown slightly below 750 K.[22–24] Further, compared to similar materials ($Cu_2ZnSnSe_4$, $E_{form} = −4.06$ eV/f.u.[80] and Cu_2ZnSnS_4, $E_{form} = −4.84$ eV/f.u.,[81] both experimentally determined through calorimetry), the formation energies of t- and o-$Cu_2CdGe(S_xSe_{1-x})_4$ are significantly lower, between −5.5 and −7.1 eV/f.u. Thus, both phases of $Cu_2CdGe(S_xSe_{1-x})_4$ may be expected to have increased stability compared to similar materials.

The decrease in lattice parameters with increasing [S] is because [S] is more electronegative than [Se] ($\chi_S = 2.6$ and $\chi_{Se} = 2.4$ on the Allen scale[82]). Substituting Se with S decreases bond lengths and contracts the cell, evidenced by Bader charge analysis (Tables II, S1 and S2 in the supplementary material), further discussed in Sec. III B 1. Table II shows charge analysis for end members, while Tables S1 and S2 in the supplementary material detail the results of the charge analysis for each unique atom in the unit cell.

From Table S3 in the supplementary material, which lists average pair distances between cations and anions in Cu_2CdGe

$(S_xSe_{1-x})_4$, one can see the minor differences between bond lengths in t- and o-$Cu_2CdGe(S_xSe_{1-x})_4$. Further, it shows that the average nearest neighbor distance involving Se in $Cu_2CdGeSe_4$ (both phases) is 2.53 Å, while the average nearest neighbor distance involving S in Cu_2CdGeS_4 (both phases) is 2.40 Å. This corresponds with the decreasing lattice parameters as well.

Simulated powder diffraction patterns for each x can be found in Fig. S1 in the supplementary material. The general heights and locations of peaks are fairly consistent with Li's aforementioned experimental observations on both t-$Cu_2CdGe(S_xSe_{1-x})_4$ ($0 \leq x \leq 0.15$) and o-$Cu_2CdGe(S_xSe_{1-x})_4$ ($0 \leq x \leq 1$).[22] Inconsistencies, the most notable being the relative heights of o-$Cu_2CdGe(S_xSe_{1-x})_4$, can be explained by the fact that our XRD was calculated for a single unit cell with consistent anion sites and a simplified treatment of finite-temperature effects. Also consistent with Li's work, we observe a consistent rightward shift of the intensity spikes as x increases due to the shrinking lattice parameters. The major intensities keep their relative locations, which show that the

TABLE II. Bader charge analysis details for tetragonal $Cu_2CdGe(S_xSe_{1-x})_4$ end members. The charge of atom i, q_i, is given in units of the elementary charge e. The charges for the tetragonal and orthorhombic structures are identical up to ±0.01e; thus, the table applies to both systems. Data on intermediate x are given in Tables S1 and S2 in the supplementary material.

-	q_{Cu}	q_{Cd}	q_{Ge}	q_{Se} or q_S
$Cu_2CdGeSe_4$	0.36	0.71	0.85	−0.57
Cu_2CdGeS_4	0.49	0.86	1.20	−0.76

models retain their structure throughout the entire range of x, despite anion substitution. Our XRD figures for t-Cu$_2$CdGe(S$_x$Se$_{1-x}$)$_4$ ($x > 0.15$) are predictive since no experimental data exist.

2. Elastic properties, stability

To study material strength and stability, we calculate the elastic constants (C_{ij}s) unique to an orthorhombic structure for every x. For consistency, we apply the orthorhombic set of strains even to the tetragonal system. Hill's averages for the bulk, shear, and Young's moduli (B, G, Y, respectively) as well as Vickers hardness (H_V) and the Debye Temperature (T_D) are listed in Table III, and the explicit values for C_{ij} are tabulated in Tables S4 and S5 in the supplementary material. Poisson's ratio (ν) was also calculated and found to be constant in x: $\nu = 0.32$. Values for B, G, and Y for t-Cu$_2$CdGeSe$_4$ and t-Cu$_2$CdGeS$_4$ are comparable to the previous DFT results.[28,35] H_V should only be considered as an order of magnitude estimation since its estimated values are less than 5 GPa. As discussed by Tian et al.,[83] the empirical formula used here ($H_V = 0.92k^{1.137}G^{0.708}$) overestimates H_V's true value when $H_V \lesssim 5$ GPa.

B, G, Y, and T_D generally increase with x although not following monotonicity. The general increase with x is due to S bonds being stronger than Se bonds—the same effect that causes lattice parameters to decrease with increasing [S], discussed in Sec. III A 1. The trendless rates that parameters increase at and the dips in strength at $x = 0.125$, $x = 0.250$ could be explained by the observation that the structures of intermediate phases have lower symmetry than the end members.

t-Cu$_2$CdGe(S$_x$Se$_{1-x}$)$_4$ is found to be elastically stronger and more heat resistant than o-Cu$_2$CdGe(S$_x$Se$_{1-x}$)$_4$. Plots of the –pCOHP in Fig. 1 (end members only) and Fig. S2 in the supplementary material (all x) show that Cu bonding states around 2 eV below the Fermi energy (E_F) are slightly stronger in t-Cu$_2$CdGe(S$_x$Se$_{1-x}$)$_4$ than in o-Cu$_2$CdGe(S$_x$Se$_{1-x}$)$_4$, which further explains t-Cu$_2$CdGe(S$_x$Se$_{1-x}$)$_4$'s superior resistance to strain and heat. Further discussion of the –pCOHP can be found in Sec. III B 2.

The directional dependence of Y is shown in Fig. 2(a) (t-phase, Y_t) and Fig. 2(b) (o-phase, Y_o). Only end members are shown for the sake of brevity. Figure S3 in the supplementary material shows the results for all x. Y_t is found to be highest along (± 1, ± 1, ± 1) directions, while Y_o is highest in only the (± 1, 0, 0) directions. Although the general Y is shown in Table III to be larger for t-Cu$_2$CdGe(S$_x$Se$_{1-x}$)$_4$ than for o-Cu$_2$CdGe(S$_x$Se$_{1-x}$)$_4$, Y_o's maximum value is twice as large as Y_t's maximum. Y_t, however, is more isotropic. Y_t is about 13% larger in the (0, 0, 1) plane than in the other two directions. Y_o's maximum values on the (0, 1, 0) and (0, 0, 1) planes are about 56% larger than its maximum on the (1, 0, 0) plane. The shape of the directionally dependent Y is directly correlated to the bonding angles in t- and o-Cu$_2$CdGe(S$_x$Se$_{1-x}$)$_4$. The tetragonal structure's bonds are oriented diagonally with respect to the model's lattice vectors, corresponding to the maxima of Y being along the diagonal directions. The orthorhombic structure has bonds directly along the a vector and also in the $b-c$ plane, which explains the calculated Y in the a direction being much higher than in the b or c directions. Y_o (Y_t) in the a, b, c (diagonal) directions is greater than Y_t (Y_o) in those directions since the orthorhombic (tetragonal) model's bonds are mostly oriented parallel (diagonal) to the lattice vectors.

Additionally, we find that all structures are mechanically stable according to the Born relations[60] between C_{ij} given in Sec. II. From indications of the C_{ij} values in Table III, we may conclude that the mechanical stability of t-Cu$_2$CdGe(S$_x$Se$_{1-x}$)$_4$ should be slightly more than that of o-Cu$_2$CdGe(S$_x$Se$_{1-x}$)$_4$ for any specific value of x. Further, both phases of Cu$_2$CdGe(S$_x$Se$_{1-x}$)$_4$ should grow in stability with increasing [S].

Finally, all structures are predicted to be dynamically stable according to the near-zero imaginary phonon frequencies. The relevant frequencies are plotted as a density of states (DOS) [Fig. S4(a) in the supplementary material for t-Cu$_2$CdGe(S$_x$Se$_{1-x}$)$_4$ and S4(b) in the supplementary material for o-Cu$_2$CdGe(S$_x$Se$_{1-x}$)$_4$]. Although in theory, any imaginary frequencies predict a dynamically unstable structure, there are indications that the ones computed by Phonopy can be attributed to approximation and numerical error. First, the largest value of the phonon DOS for any imaginary frequency is for the tetragonal $x = 0.000$ structure, which is already known experimentally to be stable. Second, the

TABLE III. Elastic parameters for tetragonal (t-) and orthorhombic (o-) Cu$_2$CdGe(S$_x$Se$_{1-x}$)$_4$. Bulk (B), shear (G), and Young's (Y) modulus as well as Vickers hardness (H_V), in units of GPa. The Debye temperature (T_D) is given in kelvin.

|	t-Cu$_2$CdGe(S$_x$Se$_{1-x}$)$_4$					o-Cu$_2$CdGe(S$_x$Se$_{1-x}$)$_4$				
x	B	G	Y	H_V	T_D	B	G	Y	H_V	T_D
0.000	57, (60)[a], (58)[b]	23, (26)[a], (22)[b]	61, (69)[a]	3	233	55	22	59	3	228
0.125	57	23	61	3	236	57	23	61	3	236
0.250	58	23	62	3	243	57	23	61	3	241
0.375	60	24	64	3	251	58	24	63	3	249
0.500	61	25	65	3	260	61	25	66	3	260
0.625	63	26	70	3	274	62	25	67	3	268
0.750	65	27	70	3	282	63	26	69	3	279
0.875	67	27	72	3	294	65	26	70	3	288
1.000	69, (70)[b]	28, (28)[b]	74	4	305	68	27	73	3	302

[a]Reference 28 (theoretical).
[b]Reference 35 (theoretical).
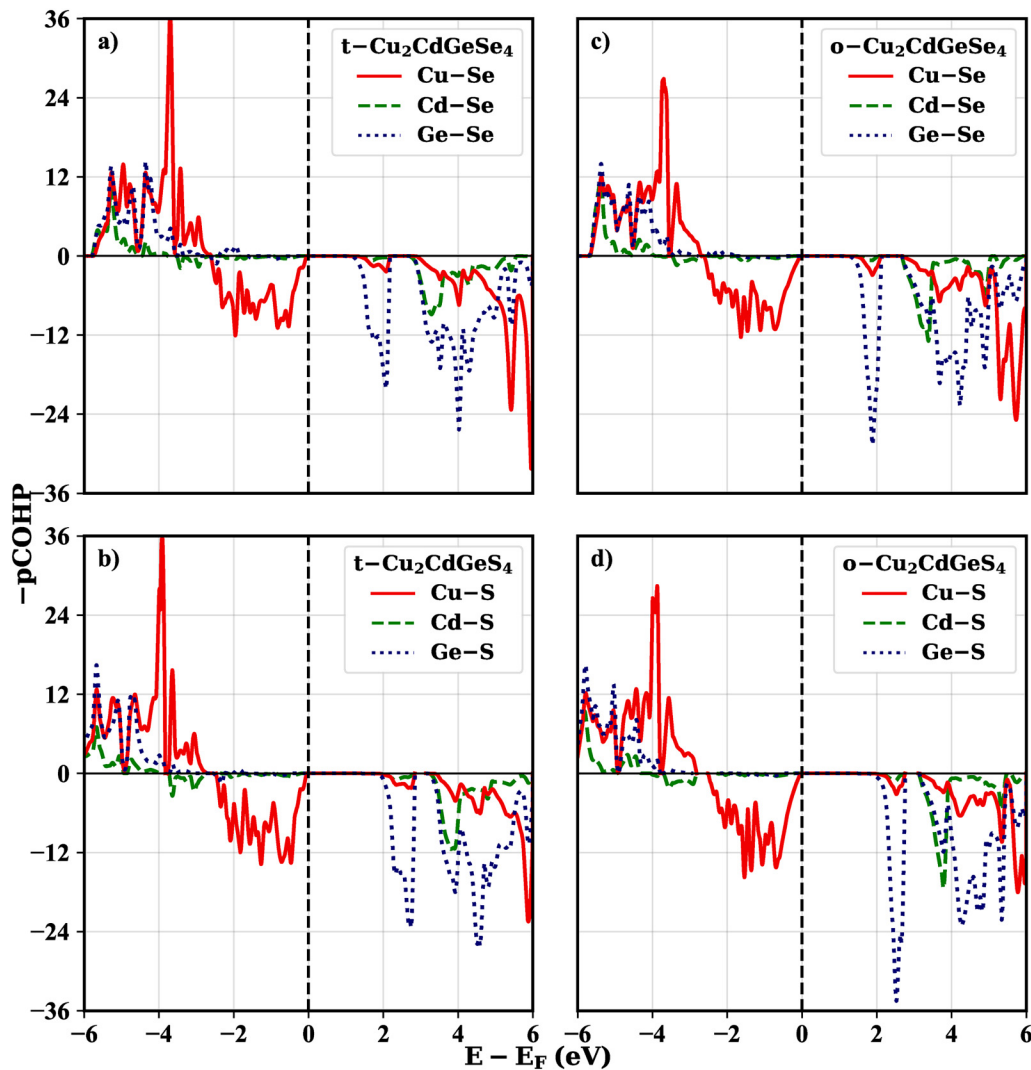
FIG. 1. (a)–(d) COHP plots for the nearest neighbor interactions in tetragonal (t-, first column) and orthorhombic (o-, second column) $Cu_2CdGeSe_4$ (top row) and Cu_2CdGeS_4 (bottom row) (a) t-$Cu_2CdGeSe_4$, (b) t-Cu_2CdGeS_4, (c) o-$Cu_2CdGeSe_4$, and (d) o-Cu_2CdGeS_4.

magnitude of the DOS for imaginary frequencies has a maximum of about 0.05 state/THz, which is orders of magnitude smaller than the DOS values for real frequencies (over 10 states/THz on average). Third, the phonon DOS always decreases as the imaginary part of the frequency increases, indicating that the error likely comes from well-known convergence issues near the Γ point.[84] Finally, the imaginary frequencies for the orthorhombic structure are very similar in magnitude to those of the tetragonal structure.

B. Optoelectronic properties

1. Bader charge analysis

Bader charge analysis shows that Se atoms in t-Cu_2CdGe $(S_xSe_{1-x})_4$ have an average excess charge of $-0.57\,e$, while S atoms

have an average excess charge of $-0.76\,e$ (where e is the elementary charge). In o-$Cu_2CdGe(S_xSe_{1-x})_4$, the charge transfer has nearly identical values of $-0.58\,e$ and $-0.76\,e$ for Se and S, respectively. Table II gives the charges for all elements in $Cu_2CdGe(S_xSe_{1-x})_4$'s end members, and Tables S1 and S2 in the supplementary material provide the full details of the charge analysis for anions over all x. Overall, substituting Se $\rightarrow$ S results in a material with more ionic character, in line with the increased mechanical strength (Sec. III A 2) and bandgap (Sec. III B 3).

2. Crystal orbital Hamiltonian population

Relative contributions of specific atom pairs' interactions to the stability of the system can be inferred from COHP data.
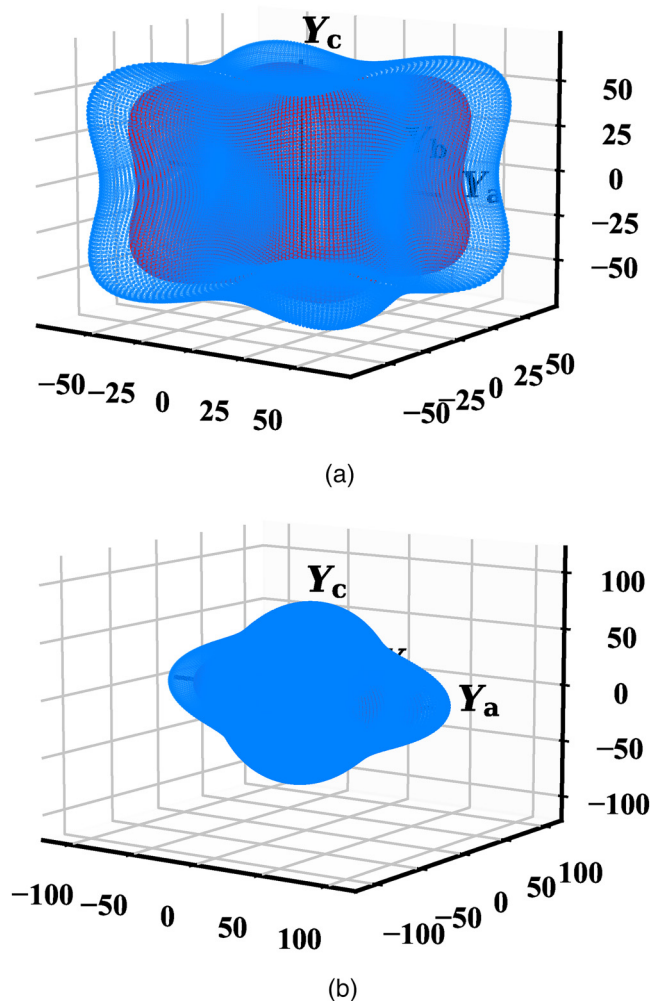
FIG. 2. (a) and (b) Directional dependence of Young's modulus Y in Cu$_2$CdGeSe$_4$ (red, inner surfaces) and Cu$_2$CdGeS$_4$ (blue, outer surfaces) for both tetragonal (a) and orthorhombic (b) phases.

FIG. 3. Bandgaps (E_g) and effective carrier masses for tetragonal (t-) and orthorhombic (o-) Cu$_2$CdGe(S$_x$Se$_{1-x}$)$_4$. Hole effective masses (m_h^*) and electron effective masses (m_e^*) are normalized to m_0—the electron rest mass. The lines through the E_g datapoints are linear best fits.

Figure 1 shows –pCOHP plots for S and Se pairs (any atom pair between 1 and 3.2 Å, i.e., only first nearest-neighbors) of t- and o-Cu$_2$CdGe(S$_x$Se$_{1-x}$)$_4$ end members. –pCOHP data for all intermediate phases can be found in Fig. S2 in the supplementary material. Cu-(Se/S) pairs are responsible for the majority of the populations, especially from energies between −2 eV and E_F. Most of the COHP in this energy range is antibonding, which coincides with the relatively small elastic strength values of Cu$_2$CdGe(S$_x$Se$_{1-x}$)$_4$. The exception is Ge-(Se/S) pairs, which are mostly bonding up until after E_F. Other than the slight differences in Ge pair bonding states near −2 eV, there are no notable differences in –pCOHP plots between t-Cu$_2$CdGe(S$_x$Se$_{1-x}$)$_4$ and o-Cu$_2$CdGe(S$_x$Se$_{1-x}$)$_4$.

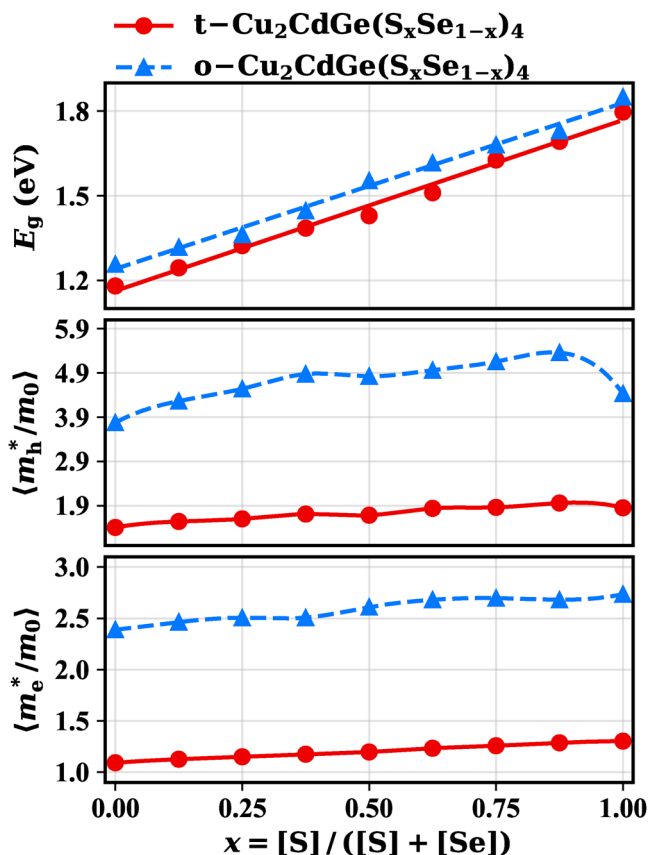The integrated total COHP (IpCOHP) was also computed. It reveals that despite the antibonding states below E_F, IpCOHP is negative until 6 eV above the fermi level. Thus, in agreement with the stability tests done with C_{ij}, Cu$_2$CdGe(S$_x$Se$_{1-x}$)$_4$ is predicted to have stable bonds for all x according to the interpretation that bond strength increases as the IpCOHP decreases below 0 eV.[76]

3. Bandgap, density of states

Calculated values for the bandgap (E_g) are shown in Fig. 3 and tabulated in Table S6 in the supplementary material. E_g for Cu$_2$CdGeSe$_4$ and Cu$_2$CdGeS$_4$ are in good agreement with external quantum efficiency (EQE, experimental) measurements[10,22,23,27,32] and previous DFT calculations.[28,33] Of the Cu-quaternary chalcogenides, the E_g of t- and o-Cu$_2$CdGeSe$_4$ is lower than average and most comparable to Cu$_2$ZnSnSe$_4$, Cu$_2$CdSnSe$_4$ Cu$_2$ZnGeSe$_4$, Cu$_2$ZnSnS$_4$, Cu$_2$CdSnS$_4$, and Cu$_2$CdSnSe$_4$,[7–9,13,16,17] which have bandgaps between 1.0 and 1.4 eV. t- and o-Cu$_2$CdGeS$_4$'s E_g are closest to Cu$_2$ZnGeS$_4$ and Cu$_2$CdSiS$_4$[8,9] with gaps between 1.8 and 2.2 eV. Intermediate x bridge the gap between the two, with E_g values similar to Cu$_2$ZnGeSe$_4$, Cu$_2$ZnSiTe$_4$, and Cu$_2$ZnGeTe$_4$.[7,10,12]
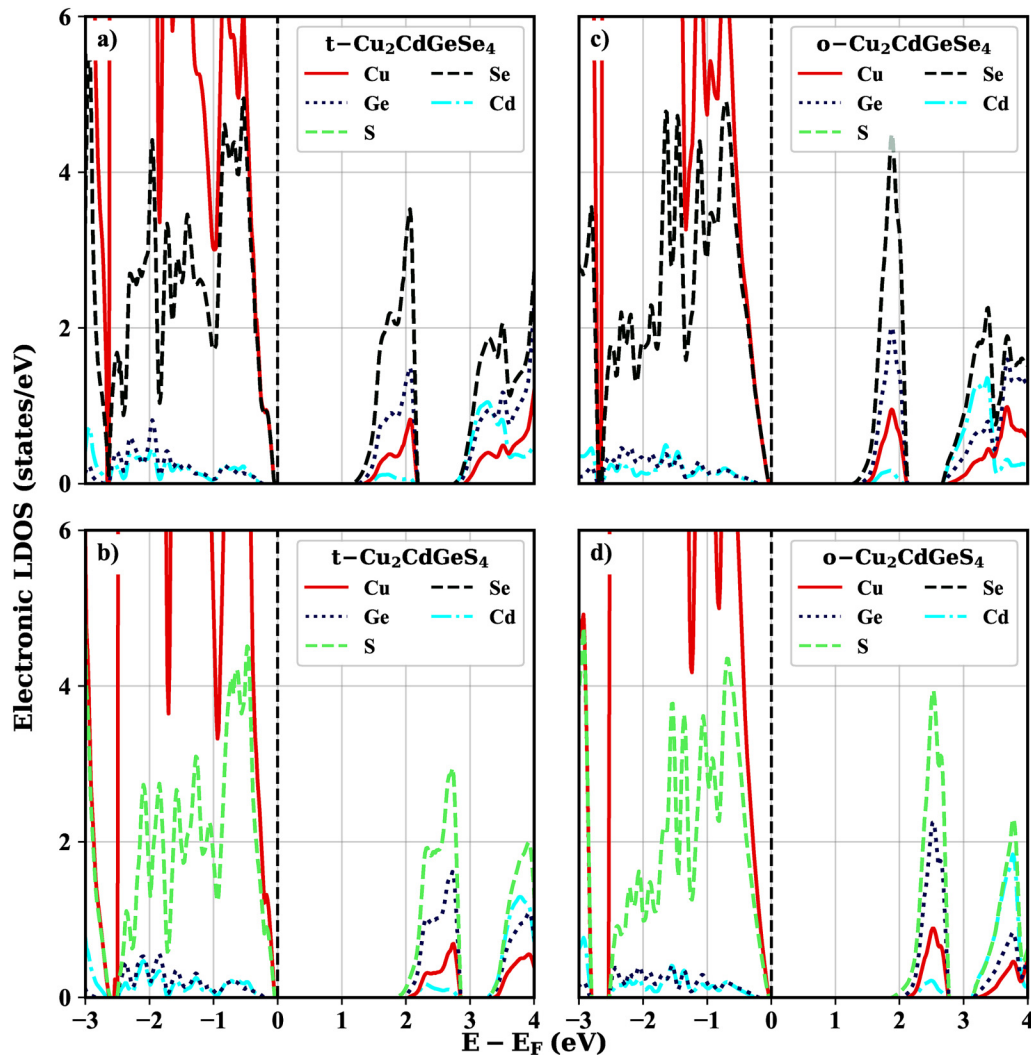
FIG. 4. (a)–(d) LDOS plots for tetragonal (t-, first column) and orthorhombic (o-, second column) Cu$_2$CdGeSe$_4$ (top row)/Cu$_2$CdGeS$_4$ (bottom row). (a) t-Cu$_2$CdGeSe$_4$, (b) t-Cu$_2$CdGeS$_4$, (c) o-Cu$_2$CdGeSe$_4$, and (d) o-Cu$_2$CdGeS$_4$.

This entire range of values sits between compounds like Cu$_2$ZnSnTe$_4$,[14] with a gap of 0.9 eV, and compounds like Cu$_2$ZnSi (S/Se)$_4$,[8,9] with gap values ranging from 2.3 (Se) up to 3.3 (S) eV. Thus, this alloy system is very suitable for absorbing the relevant part of the AM1.5 solar spectrum.[85] It could lead to a continuous concentration graded (varying x) absorber layer, which could act as a tandem layer made up of this single alloy system. Both phases of Cu$_2$CdGe(S$_x$Se$_{1-x}$)$_4$ are found to have a direct gap for all x. In general, the bandgap widens with increasing x since S has a stronger ionic character than Se. Additionally, the linear E_g vs x relationship for o-Cu$_2$CdGe(S$_x$Se$_{1-x}$)$_4$ agrees with EQE measurements of Li et al.[22] Quantitatively, our E_g values are consistently about 0.1 eV below the measurements of Li et al. Such level of agreement is

expected for computations performed with the hybrid HSE06 functional.[47,63]

E_g of t-Cu$_2$CdGe(S$_x$Se$_{1-x}$)$_4$ is smaller than that of o-Cu$_2$CdGe (S$_x$Se$_{1-x}$)$_4$ by 0.08 eV on average. t-Cu$_2$CdGe(S$_x$Se$_{1-x}$)$_4$ also shows a slight deviation in E_g around $x = 0.500$, where the gap drops below what a linear trend would suggest. The E_gs' of Cu$_2$CdGe (S$_x$Se$_{1-x}$)$_4$ looks as though they oscillate around the linear best fit, but the deviations are far less than the precision of the computations (previously approximated as 0.1 eV on account of the bulk material's configurational entropy being simplified in computations).

The DOS graphs in Figs. 4 and S5 in the supplementary material show that, regardless of x, Cu is consistently the major contributor to the location of the VBM in Cu$_2$CdGe(S$_x$Se$_{1-x}$)$_4$.

Further analysis of the l-decomposed PDOS reveals that the Cu states in question are almost exclusively $3d$ states (not shown in Fig. 4 for the sake of brevity). Se or S contributes significantly to the VBM as well, depending on x. As for the location of the CBM, it is determined mostly by the anions.

4. Effective masses

Figure 3 shows the average conductivity effective masses of holes (m_h^*/m_0) and electrons (m_e^*/m_0) for $T = 300$ K. Additionally, Table S7 in the supplementary material lists explicit values for m_h^*/m_0 and m_e^*/m_0 along a few specific reciprocal-space lines calculated with the standard parabolic band approximation. Effective masses are effective indicators of material conductivity

that can be computed without the complicated modeling of charge carrier scattering. Small effective masses are generally associated with high conductivity.

t-Cu$_2$CdGe(S$_x$Se$_{1-x}$)$_4$'s effective masses are consistently lower than o-Cu$_2$CdGe(S$_x$Se$_{1-x}$)$_4$'s for both electrons and holes. In both cases, the tetragonal system's masses are about half that of the orthorhombic system's for any given value of x. Thus, we predict that the tetragonal system should have better transport properties than the orthorhombic system. Specifically, t-Cu$_2$CdGe(S$_x$Se$_{1-x}$)$_4$'s electrons are predicted to be only slightly heavier than that of a resting electron at room temperature, and its holes between one and two times heavier than a resting electron.

Comparing Fig. 3 with Table S7 in the supplementary material provides information on the directional dependence of
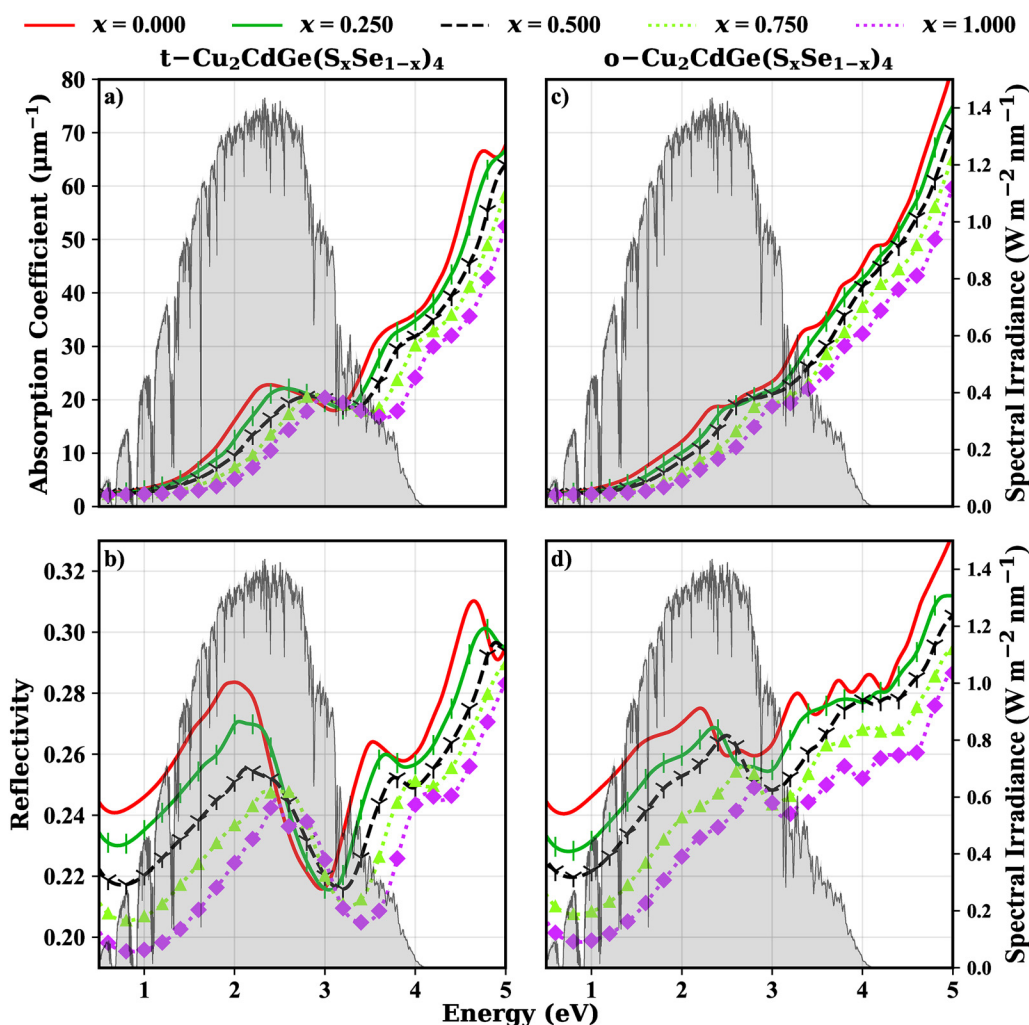

FIG. 5. (a)–(d) Optical properties for tetragonal (t-, first column) and orthorhombic (o-, second column) Cu$_2$CdGe(S$_x$Se$_{1-x}$)$_4$ in the visible/near UV range for PV applications. Symbols on lines are for clarity of presentation only. Optical response functions are found to be independent of orientation. Gray background function is the AM 1.5 solar spectrum, which has corresponding values labeled on the right side of the plots. (a) Absorption coefficient for t-Cu$_2$CdGe(S$_x$Se$_{1-x}$)$_4$, (b) reflectivity for t-Cu$_2$CdGe (S$_x$Se$_{1-x}$)$_4$, (c) absorption coefficient for o-Cu$_2$CdGe(S$_x$Se$_{1-x}$)$_4$, and (d) reflectivity for o-Cu$_2$CdGe(S$_x$Se$_{1-x}$)$_4$.

conductivity. Electron masses along t- and o-Cu$_2$CdGe(S$_x$Se$_{1-x}$)$_4$'s lattice directions are nearly identical, yet their conductivity masses are significantly different. This indicates that a large portion of o-Cu$_2$CdGe(S$_x$Se$_{1-x}$)$_4$'s electron conductivity mass comes from directions diagonal to its lattice vectors. Additionally, holes in both phases of Cu$_2$CdGe(S$_x$Se$_{1-x}$)$_4$ exhibit lower effective masses in the (001) direction than in the (100) or (010) directions. This effect is particularly large for o-Cu$_2$CdGe(S$_x$Se$_{1-x}$)$_4$'s holes, where the masses in the (001) directions are about half that of the masses in the (100) or (010) directions.

5. Absorption coefficient, reflectivity

Absorption coefficient (α) and reflectivity functions (R) between 0.5 and 5.0 eV for Cu$_2$CdGe(S$_x$Se$_{1-x}$)$_4$ are shown in Figs. 5 and S6 in the supplementary material. These functions are imperative for evaluating the potential of materials to be used as photoabsorbers. Each of the six components (xx, yy, zz, yz, zx, xy) of the complex relative dielectric functions (plotted in Fig. S7 in the supplementary material) deviates from their average by less than 10^{-8}, so the optical response functions of Cu$_2$CdGe(S$_x$Se$_{1-x}$)$_4$ are isotropic. In general, the features of α and R decrease in max intensity and are blue-shifted with increasing x, but are otherwise unchanged within any given phase.

The αs for both t-Cu$_2$CdGe(S$_x$Se$_{1-x}$)$_4$ and o-Cu$_2$CdGe(S$_x$Se$_{1-x}$)$_4$ generally decrease with x, t-Cu$_2$CdGe(S$_x$Se$_{1-x}$)$_4$ more so than o-Cu$_2$CdGe(S$_x$Se$_{1-x}$)$_4$. Additionally, they are comparable to other common PV absorber materials.[66,67] Between photon energies of 1.8 and 2.8 eV (the peak of the standard AM 1.5 solar spectrum),[85] Si and CdTe have maximum (minimum) values of $\alpha(R)$ of 15 μm^{-1} (0.33) and 13 μm^{-1} (0.18), respectively.[67,86] Within the same range, t-Cu$_2$CdGe(S$_x$Se$_{1-x}$)$_4$'s maximum αs exceeds that of both Si and CdTe for every value of x. The same is true of o-Cu$_2$CdGe(S$_x$Se$_{1-x}$)$_4$'s maximum values of α, but only for $x \leq 0.750$. For higher values of x, the o-phase's maximum α are between Si and CdTe's values. The minimum values of R for both phases of Cu$_2$CdGe(S$_x$Se$_{1-x}$)$_4$ are consistently lower than Si's, but higher than CdTe's.

t-Cu$_2$CdGe(S$_x$Se$_{1-x}$)$_4$ has a local peak in absorption between 2.3 and 3.0 eV (depending on x), but o-Cu$_2$CdGe(S$_x$Se$_{1-x}$)$_4$ has no such peak. Instead, α levels out for a small range of energies before continuing to climb as the energy nears UV. t-Cu$_2$CdGe(S$_x$Se$_{1-x}$)$_4$ also has a small energy window near 3 eV where the local absorption coefficient is higher for large x than for small x. The difference in α's behavior between lattice types is consistent with the density of states (Figs. 4 and S5 in the supplementary material) for the two phases: the conduction bands of both systems consist of occupiable states from the CBM up to about 1 eV above the CBM, followed by a gap (a bandgap, *not* the fundamental gap E_g), and then more occupiable states at higher energies. This gap is larger in the t-phase than it is in the o-phase, so absorption at these energies is expected to be reduced for the t-phase compared to the o-phase. In t-Cu$_2$CdGe(S$_x$Se$_{1-x}$)$_4$, the gap happens to be large enough to cause a drop in absorption, whereas in o-Cu$_2$CdGe(S$_x$Se$_{1-x}$)$_4$, the absorption only flatlines since its gap is smaller.

Values for R are mild—between 20% and 30%. For t-Cu$_2$CdGe(S$_x$Se$_{1-x}$)$_4$, R of each x peak at slightly lower energies than their respective αs peak. Further, R's local minima for each x correspond to α's local minima. o-Cu$_2$CdGe(S$_x$Se$_{1-x}$)$_4$'s R does not seem to be as closely related to its α, and its local minima are less pronounced. The R for t-Cu$_2$CdGe(S$_x$Se$_{1-x}$)$_4$ varies fairly smoothly with x and E for the energy range shown, but o-Cu$_2$CdGe (S$_x$Se$_{1-x}$)$_4$'s R starts to become less predictable after 2.5 eV.

Considering both α and R, both phases of Cu$_2$CdGe(S$_x$Se$_{1-x}$)$_4$ are expected to perform better than, or at least comparable to, current absorber materials such as Si and CdTe. Thus, they should be good candidates for general purpose photon absorbers. The t-phase's peak in absorption could also be exploited in certain situations where incoming light is more monochromatic than usual. For example, the α of zincblende CdTe$_{1-x}$Se$_x$ has local minima where (low x) t-Cu$_2$CdGe(S$_x$Se$_{1-x}$)$_4$'s α has local maxima, and vice versa.[67] These two absorbers, then, could be an efficient pair for tandem solar cells.

IV. CONCLUSION

The intermediate phases, ($0 < x < 1$), of the Cu$_2$CdGe (S$_x$Se$_{1-x}$)$_4$ system were studied using first principles computations. For both t- and o- phases, we systematically calculated the structural, energetic, elastic, and optoelectronic properties by varying x. Our results for end members agree well with the available results from experiment and theory. Also, our intermediate structures agree with experiments of Li *et al.*,[22] encouraging confidence that our intermediate phase calculations are physically relevant.

We predict that material stability, strength, and resistance to heat increases with [S]. t-Cu$_2$CdGe(S$_x$Se$_{1-x}$)$_4$'s aforementioned properties are generally stronger than o-Cu$_2$CdGe(S$_x$Se$_{1-x}$)$_4$'s. Structural properties are affected much more by x than by the crystal system. In terms of structural properties, t-Cu$_2$CdGe(S$_x$Se$_{1-x}$)$_4$ is theoretically a better choice than o-Cu$_2$CdGe(S$_x$Se$_{1-x}$)$_4$ for PV applications on account of its higher predicted strength. However, a limiting factor could be the fact that Cu$_2$CdGeS$_4$ is only known to exist in the orthogonal phase, creating difficulty to synthesize t-Cu$_2$CdGe(S$_x$Se$_{1-x}$)$_4$ with high [S] by extant methods.

We predict that the E_g response of Cu$_2$CdGe(S$_x$Se$_{1-x}$)$_4$ is linear in x and that t-Cu$_2$CdGe(S$_x$Se$_{1-x}$)$_4$ has a smaller E_g than o-Cu$_2$CdGe(S$_x$Se$_{1-x}$)$_4$ by about 0.08 eV for any given x. This results in slightly different ranges of x well suited for single-junction solar cells: $0.000 \leq x \leq 0.375$ and $0.000 \leq x \leq 0.250$ for t- and o-Cu$_2$CdGe(S$_x$Se$_{1-x}$)$_4$, respectively. Other x alloys could be used in tandem solar cells since E_g approaches 2.0 eV for high [S] in both phases. Effective mass calculations indicate that there is a heavy dependence of hole mobility on direction—charge is expected to move more freely in the c direction than in either the a or b directions. Further, t-Cu$_2$CdGe(S$_x$Se$_{1-x}$)$_4$ is expected to exhibit superior conductivity compared to o-Cu$_2$CdGe(S$_x$Se$_{1-x}$)$_4$ on account of the tetragonal phase's lower conductivity masses. Finally, t-Cu$_2$CdGe (S$_x$Se$_{1-x}$)$_4$ is expected to have a local peak in its α at around 2.5 eV and a peak in R at a slightly lower energy. o-Cu$_2$CdGe(S$_x$Se$_{1-x}$)$_4$ has less pronounced optical features, but the averages of its α and R are comparable to the t-phase.

The results discussed here provide useful insight into the potential for Cu$_2$CdGe(S$_x$Se$_{1-x}$)$_4$ as a PV absorber material. Based on our results, t-Cu$_2$CdGe(S$_x$Se$_{1-x}$)$_4$ is predicted to be a material with a E_g similar to o-Cu$_2$CdGe(S$_x$Se$_{1-x}$)$_4$, but with stronger elastic

properties and better charge mobility. Thus, future research into this material could focus on t-$Cu_2CdGe(S_xSe_{1-x})_4$ as a more resilient alternative to o-$Cu_2CdGe(S_xSe_{1-x})_4$.

SUPPLEMENTARY MATERIAL

See the supplementary material for numerical values of effective Bader charges (Tables S1 and S2), bond counts and lengths (Table S3), elastic constants (Tables S4 and S5), bandgaps (Table S6), and effective masses (Table S7) for both phases and all values of x. Additionally, graphs of simulated x-ray diffraction patterns (Fig. S1), COHP (Fig. S2), directional dependence of Young's modulus (Fig. S3), phonon density of states (Fig. S4), electronic density of states (Fig. S5), optical response functions (Fig. S6), and dielectric functions (Fig. S7) for both phases and all values of x are given.

ACKNOWLEDGMENTS

AUTHOR DECLARATIONS

Conflict of Interest

The authors have no conflicts to disclose.

DATA AVAILABILITY

The data that support the findings of this study are available within the supplementary material or from the corresponding author upon reasonable request.

REFERENCES

[1]W. Wang, M. T. Winkler, O. Gunawan, T. Gokmen, T. K. Todorov, Y. Zhu, and D. B. Mitzi, "Device characteristics of CZTSSe thin-film solar cells with 12.6% efficiency," Adv. Energy Mater. **4**, 1301465 (2014).

[2]M. T. Winkler, W. Wang, O. Gunawan, H. J. Hovel, T. K. Todorov, and D. B. Mitzi, "Optical designs that improve the efficiency of $Cu_2ZnSn(S,Se)_4$ solar cells," Energy Environ. Sci. **7**, 1029 (2014).

[3]T. K. Todorov, J. Tang, S. Bag, O. Gunawan, T. Gokmen, Y. Zhu, and D. B. Mitzi, "Beyond 11% efficiency: Characteristics of state-of-the-art $Cu_2ZnSn(S,Se)_4$ solar cells," Adv. Energy Mater. **3**, 34 (2013).

[4]I. Repins, C. Beall, N. Vora, C. DeHart, D. Kuciauskas, P. Dippo, B. To, J. Mann, W.-C. Hsu, A. Goodrich, and R. Noufi, "Co-evaporated $Cu_2ZnSnSe_4$ films and devices," Sol. Energy Mater. Sol. Cells **101**, 154 (2012).

[5]W. Yang, H.-S. Duan, B. Bob, H. Zhou, B. Lei, C.-H. Chung, S.-H. Li, W. W. Hou, and Y. Yang, "Novel solution processing of high-efficiency earth-abundant $Cu_2ZnSn(S,Se)_4$ solar cells," Adv. Mater. **24**, 6323 (2012).

[6]L. Grenet, S. Bernardi, D. Kohen, C. Lepoittevin, S. Noël, N. Karst, A. Brioude, S. Perraud, and H. Mariette, "$Cu_2ZnSn(S_{1-x}Se_x)_4$ based solar cell produced by selenization of vacuum deposited precursors," Sol. Energy Mater. Sol. Cells **101**, 11 (2012).

[7]H. Matsushita, T. Maeda, A. Katsui, and T. Takizawa, "Thermal analysis and synthesis from the melts of Cu-based quaternary compounds Cu-III-IV-VI$_4$ and Cu_2-II-IV-VI$_4$ (II = Zn, Cd; III = Ga, In; IV = Ge, Sn; VI = Se)," J. Cryst. Growth **7**, 416–422 (2000).

[8]D. M. Schleich and A. Wold, "Optical and electrical properties of quarternary chalcogenides," Mater. Res. Bull. **12**, 111 (1977).

[9]G. Yao, H. Shen, E. Honig, R. Kershaw, K. Dwight, and A. Wold, "Preparation and characterization of the quaternary chalcogenides $Cu_2B(II)C(IV)X_4$ [B (II) = Zn, Cd; C(IV) = Si, Ge; X = S, Se]," Solid State Ionics **24**, 249 (1987).

[10]H. Matsushita, T. Ichikawa, and A. Katsui, "Structural, thermodynamical and optical properties of Cu_2-II-IV-VI$_4$ quaternary compounds," J. Mater. Sci. **40**, 2003 (2005).

[11]O. V. Parasyuk, I. D. Olekseyuk, and L. V. Piskach, "X-ray powder diffraction refinement of $Cu_2ZnGeTe_4$ structure and phase diagram of the Cu_2GeTe_3-ZnTe system," J. Alloys Compd. **397**, 169 (2005).

[12]L. Nieves, G. Delgado, G. Marcano, C. Power, S. Lopex-Rivera, and C. Rincon, "Structural characterization of the high-temperature modification of the $Cu_2ZnGeTe_4$ quaternary semiconductor compound," Phys. Status Solidi B **253**, 1195–1201 (1972).

[13]C. Steinhagen, M. G. Panthani, V. Akhavan, B. Goodfellow, B. Koo, and B. A. Korgel, "Synthesis of Cu_2ZnSnS_4 nanocrystals for use in low-cost photovoltaics," J.: Am. Chem. Soc. **131**, 12554 (2009).

[14]D. Pareek, K. R. Balasubramaniam, and P. Sharma, "Synthesis and characterization of kesterite $Cu_2ZnSnTe_4$ via ball-milling of elemental powder precursors," RSC Adv. **6**, 68754 (2016).

[15]V. G. Gurtova, T. V. Shelkovaya, and V. A. Chumak, "Structural Study of the $Cu_2CdSn_{1-x}Si_xSe_4$ System," Mater. Int. Sci. Tech. Conf. 257–260 (2019).

[16]Nanotechnology and Catalysis Research Center (NANOCAT), University of Malaya, 50603 Kuala Lumpur, Malaysia and Y. Al-Douri, Synthesis and characterization of Cu_2CdSnS_4 quaternary alloy nanostructures, Int. J. Electrochem. Sci. **13**, 6693 (2018).

[17]M.-L. Liu, I.-W. Chen, F.-Q. Huang, and L.-D. Chen, "Improved thermoelectric properties of Cu-doped quaternary chalcogenides of $Cu_2CdSnSe_4$," Adv. Mater. **21**, 3808 (2009).

[18]C. Yan, K. Sun, J. Huang, S. Johnston, F. Liu, B. P. Veettil, K. Sun, A. Pu, F. Zhou, J. A. Stride, M. A. Green, and X. Hao, "Beyond 11% efficient sulfide kesterite $Cu_2ZnxCd_{1-x}SnS_4$ solar cell: Effects of cadmium alloying," ACS Energy Lett. **2**, 930 (2017).

[19]X. Li, M. Pilvet, K. Timmo, M. Grossberg, M. Danilson, V. Mikli, and M. Kauk-Kuusik, "Effect of absorber surface modification on the optoelectronic properties of $Cu_2CdGeSe_4$ solar cells," Thin Solid Films **697**, 137822 (2020).

[20]M. Grossberg, T. Raadik, J. Krustok, M. Kauk-Kuusik, K. Timmo, R. Kaupmees, V. Mikli, and A. Mere, "Optical and structural properties of orthorhombic and tetragonal polymorphs of $Cu_2CdGeSe_4$," Thin Solid Films **666**, 44 (2018).

[21]T. Gokmen, O. Gunawan, T. K. Todorov, and D. B. Mitzi, "Band tailing and efficiency limitation in kesterite solar cells," Appl. Phys. Lett. **103**, 103506 (2013).

[22]X. Li, M. Pilvet, K. Timmo, M. Grossberg, V. Mikli, and M. Kauk-Kuusik, "The effect of S/Se ratio on the properties of $Cu_2CdGe(S_xSe_{1-x})_4$ microcrystalline powders for photovoltaic applications," Sol. Energy **209**, 646 (2020).

[23]M. Kauk-Kuusik, X. Li, M. Pilvet, K. Timmo, M. Grossberg, T. Raadik, M. Danilson, V. Mikli, M. Altosaar, J. Krustok, and J. Raudoja, "Study of $Cu_2CdGeSe_4$ monograin powders synthesized by molten salt method for photovoltaic applications," Thin Solid Films **666**, 15 (2018).

[24]L. D. Gulay, Y. E. Romanyuk, and O. V. Parasyuk, "Crystal structures of low- and high-temperature modifications of $Cu_2CdGeSe_4$," J. Alloys Compd. **5**, 193–197 (2002).

[25]L. P. Marushko, L. V. Piskach, O. V. Parasyuk, I. D. Olekseyuk, S. V. Volkov, and V. I. Pekhnyo, "The reciprocal system $Cu_2GeS_3 + 3CdSe \Leftrightarrow Cu_2GeSe_3 + 3CdS$," J. Alloys Compd. **473**, 94 (2009).

[26]S. Huang, J. Zai, D. Ma, Q. He, Y. Liu, Q. Qiao, and X. Qian, "Colloidal synthesis of wurtz-stannite Cu_2CdGeS_4 nanocrystals with high catalytic activity toward iodine redox couples in dye-sensitized solar cells," Chem. Commun. **52**, 10866 (2016).

[27]J. Krustok, T. Raadik, X. Li, M. Kauk-Kuusik, K. Timmo, S. Oueslati, and M. Grossberg, "Study of point defects in wide-bandgap Cu_2CdGeS_4 microcrystals by temperature and laser power dependent photoluminescence spectroscopy," J. Phys. D: Appl. Phys. **53**, 275102 (2020).

[28]T. V. Vu, A. A. Lavrentyev, B. V. Gabrelian, K. D. Pham, C. V. Nguyen, K. C. Tran, H. L. Luong, M. Batouche, O. V. Parasyuk, and O. Y. Khyzhun, "Electronic, optical and elastic properties of $Cu_2CdGeSe_4$: A first-principles study," J. Electron. Mater. **48**, 705 (2019).

[29]M. I. Ziane, D. Ouadjaout, M. Tablaoui, R. Nouri, W. Zermane, A. Djelloul, H. Bennacer, A. Mokrani, M. Hadjab, and H. Abid, "First-principle computed structural and thermodynamic properties of $Cu_2ZnSn(Sx Se_{1-x})_4$ pentanary solid solution," J. Electron. Mater. **48**, 6991 (2019).

[30]K. Shen, G. Jia, X. Zhang, and Z. Jiao, "The electronic structure, elastic and optical properties of $Cu_2ZnGe(Sex S_{1-x})_4$ alloys: Density functional calculations," Mol. Phys. **114**, 2948 (2016).

[31]M. G. Brik, I. V. Kityk, O. V. Parasyuk, and G. L. Myronchuk, "Photoinduced features of energy bandgap in quaternary Cu_2CdGeS_4 crystals," J. Phys.: Condens. Matter **25**, 505802 (2013).

[32]M. G. Brik, O. V. Parasyuk, G. L. Myronchuk, and I. V. Kityk, "Specific features of band structure and optical anisotropy of $Cu_2CdGeSe_4$ quaternary compounds," Mater. Chem. Phys. **147**, 155 (2014).

[33]Y. Zhang, X. Sun, P. Zhang, X. Yuan, F. Huang, and W. Zhang, "Structural properties and quasiparticle band structures of Cu-based quaternary semiconductors for photovoltaic applications," J. Appl. Phys. **111**, 063709 (2012).

[34]P. P. Gunaicha, S. Gangam, J. L. Roehl, and S. V. Khare, "Structural, energetic and elastic properties of $Cu_2ZnSn(Sx Se_{1-x})_4$ (X = 1, 0.75, 0.5, 0.25, 0) alloys from first-principles computations," Sol. Energy **102**, 276 (2014).

[35]S. Hasan, K. Baral, N. Li, and W.-Y. Ching, "Structural and physical properties of 99 complex bulk chalcogenides crystals using first-principles calculations," Sci. Rep. **11**, 9921 (2021).

[36]G. Kresse and J. Hafner, "*Ab initio* molecular dynamics for liquid metals," Phys. Rev. B **47**, 558 (1993).

[37]G. Kresse and J. Furthmüller, "Efficient iterative schemes for *Ab initio* total-energy calculations using a plane-wave basis Set," Phys. Rev. B **54**, 11169 (1996).

[38]N. J. Szymanski, I. Khatri, J. G. Amar, D. Gall, and S. V. Khare, "Unconventional superconductivity in 3d rocksalt transition metal carbides," J. Mater. Chem. C **7**, 12619 (2019).

[39]J. P. Perdew, K. Burke, and M. Ernzerhof, "Generalized gradient approximation made simple," Phys. Rev. Lett. **77**, 3865 (1996).

[40]P. E. Blöchl and P. A.-W. Method, Phys. Rev. B **50**, 17953 (1994).

[41]H. J. Monkhorst and J. D. Pack, "Special points for Brillouin-zone integrations," Phys. Rev. B **13**, 5188 (1976).

[42]V. Adhikari, Z. T. Y. Liu, N. J. Szymanski, I. Khatri, D. Gall, P. Sarin, and S. V. Khare, "First-principles study of mechanical and magnetic properties of transition metal (M) nitrides in the cubic M_4N structure," J. Phys. Chem. Solids **120**, 197 (2018).

[43]Z. T. Y. Liu, N. J. Podraza, S. V. Khare, and P. Sarin, "Transparency enhancement for $SrVO_3$ by $SrTiO_3$ mixing: A first-principles study," Comput. Mater. Sci. **144**, 139 (2018).

[44]A. Jain, S. P. Ong, G. Hautier, W. Chen, W. D. Richards, S. Dacek, S. Cholia, D. Gunter, D. Skinner, G. Ceder, and K. A. Persson, "Commentary the materials project a materials genome approach to accelerating materials innovation," APL Mater. **1**, 011002 (2013).

[45]K. Momma and F. Izumi, "VESTA3 for three-dimensional visualization of crystal, volumetric and morphology data," J. Appl. Crystallogr. **44**, 1272 (2011).

[46]N. Jiang, J. L. Roehl, S. V. Khare, D. G. Georgiev, and A. H. Jayatissa, "An *Ab initio* computational study of pure Zn_3N_2 and Its native point defects and dopants Cu, Ag and Au," Thin Solid Films **564**, 331 (2014).

[47]N. J. Szymanski, L. N. Walters, O. Hellman, D. Gall, and S. V. Khare, "Dynamical stabilization in delafossite nitrides for solar energy conversion," J. Mater. Chem. A **6**, 20852 (2018).

[48]G. Henkelman, A. Arnaldsson, and H. Jónsson, "A fast and robust algorithm for Bader decomposition of charge density," Comput. Mater. Sci. **36**, 354 (2006).

[49]E. Sanville, S. D. Kenny, R. Smith, and G. Henkelman, "Improved grid-based algorithm for Bader charge allocation," J. Comput. Chem. **28**, 899 (2007).

[50]W. Tang, E. Sanville, and G. Henkelman, "A grid-based Bader analysis algorithm without lattice bias," J. Phys.: Condens. Matter **21**, 084204 (2009).

[51]M. Yu and D. R. Trinkle, "Accurate and efficient algorithm for Bader charge integration," J. Chem. Phys. **134**, 064111 (2011).

[52]V. Adhikari, N. J. Szymanski, I. Khatri, D. Gall, and S. V. Khare, "First principles investigation into the phase stability and enhanced hardness of TiN-ScN and TiN-YN alloys," Thin Solid Films **688**, 137284 (2019).

[53]X. Zhou, D. Gall, and S. V. Khare, "Mechanical properties and electronic structure of anti-ReO_3 structured cubic nitrides, M_3N, of d block transition metals M: An *Ab initio* study," J. Alloys Compd. **595**, 80 (2014).

[54]Z. T. Y. Liu, D. Gall, and S. V. Khare, "Electronic and bonding analysis of hardness in pyrite-type transition-metal pernitrides," Phys. Rev. B **90**, 134102 (2014).

[55]I. Efthimiopoulos, I. Khatri, Z. T. Y. Liu, S. V. Khare, P. Sarin, V. Tsurkan, A. Loidl, D. Zhang, and Y. Wang, "Universal link of magnetic exchange and structural behavior under pressure in chromium spinels," Phys. Rev. B **97**, 184435 (2018).

[56]P. Ravindran, L. Fast, P. A. Korzhavyi, B. Johansson, J. Wills, and O. Eriksson, "Density functional theory for calculation of elastic properties of orthorhombic crystals: Application to $TiSi_2$," J. Appl. Phys. **84**, 4891 (1998).

[57]Z. Wu, E. Zhao, H. Xiang, X. Hao, X. Liu, and J. Meng, "Crystal structures and elastic properties of superhard IrN_2 and IrN_3 from first principles," Phys. Rev. B **76**, 054115 (2007).

[58]I. Khatri, N. J. Szymanski, B. B. Dumre, J. G. Amar, D. Gall, and S. V. Khare, "Correlating structure and orbital occupation with the stability and mechanical properties of 3d transition metal carbides," J. Alloys Compd. **891**, 161866 (2022).

[59]C. Chen, L. Liu, Y. Wen, Y. Jiang, and L. Chen, "Elastic properties of orthorhombic $YBa_2Cu_3O_7$ under pressure," Crystals **9**, 497 (2019).

[60]F. Mouhat and F.-X. Coudert, "Necessary and sufficient elastic stability conditions in various crystal systems," Phys. Rev. B **90**, 224104 (2014).

[61]A. Togo and I. Tanaka, "First principles phonon calculations in materials science," Scr. Mater. **108**, 1 (2015).

[62]A. V. Krukau, O. A. Vydrov, A. F. Izmaylov, and G. E. Scuseria, "Influence of the exchange screening parameter on the performance of screened hybrid functionals," J. Chem. Phys. **125**, 224106 (2006).

[63]N. J. Szymanski, Z. T. Y. Liu, T. Alderson, N. J. Podraza, P. Sarin, and S. V. Khare, "Electronic and optical properties of vanadium oxides from first principles," Comput. Mater. Sci. **146**, 310 (2018).

[64]R. Deng, B. D. Ozsdolay, P. Y. Zheng, S. V. Khare, and D. Gall, "Optical and transport measurement and first-principles determination of the ScN band gap," Phys. Rev. B **91**, 045104 (2015).

[65]N. J. Szymanski, V. Adhikari, M. A. Willard, P. Sarin, D. Gall, and S. V. Khare, "Prediction of improved magnetization and stability in $Fe_{16}N_2$ through alloying," J. Appl. Phys. **126**, 093903 (2019).

[66]B. B. Dumre, D. Gall, and S. V. Khare, "Stability, and electronic and optical properties of ternary nitride phases of $MgSnN_2$: A first-principles study," J. Phys. Chem. Solids **153**, 110011 (2021).

[67]B. B. Dumre, N. J. Szymanski, V. Adhikari, I. Khatri, D. Gall, and S. V. Khare, "Improved optoelectronic properties in $CdSex Te_{1-x}$ through controlled composition and short-range order," Sol. Energy **194**, 742 (2019).

[68]P. E. Blöchl, O. Jepsen, and O. K. Andersen, "Improved tetrahedron method for Brillouin-zone integrations," Phys. Rev. B **49**, 16223 (1994).

[69]Z. T. Y. Liu, X. Zhou, D. Gall, and S. V. Khare, "First-Principles investigation of the structural, mechanical and electronic properties of the NbO-structured 3d, 4d and 5d transition metal nitrides," Comput. Mater. Sci. **84**, 365 (2014).

[70]Z. T. Y. Liu, X. Zhou, S. V. Khare, and D. Gall, "Structural, mechanical and electronic properties of 3d transition metal nitrides in cubic zincblende, rocksalt and cesium chloride structures: A first-principles investigation," J. Phys.: Condens. Matter **26**, 025404 (2014).

[71]V. L. Deringer, A. L. Tchougréeff, and R. Dronskowski, "Crystal orbital Hamilton population (COHP) analysis as projected from plane-wave basis sets," J. Phys. Chem. A **115**, 5461 (2011).

[72]S. Maintz, V. L. Deringer, A. L. Tchougréeff, and R. Dronskowski, "Analytic projection from plane-wave and PAW wavefunctions and application to chemical-bonding analysis in solids," J. Comput. Chem. **34**, 2557 (2013).

[73]S. Maintz, V. Deringer, A. Tchougreeff, and R. Dronskowski, "LOBSTER: A tool to extract chemical bonding from plane-wave based DFT," J. Comput. Chem. **37**, 1030 (2016).

[74]S. Maintz, M. Esser, and R. Dronskowski, "Efficient rotation of local basis functions using real spherical harmonics," Acta Phys. Pol. B **47**, 1165 (2016).

[75]R. Nelson, C. Ertural, J. George, V. L. Deringer, G. Hautier, and R. Dronskowski, "LOBSTER: Local orbital projections, atomic charges, and chemical-bonding analysis from projector-augmented-wave-based density-functional theory," J. Comput. Chem. **41**, 1931 (2020).

[76]R. Dronskowski and P. E. Bloechl, "Crystal orbital Hamilton populations (COHP): Energy-resolved visualization of chemical bonding in solids based on density-functional calculations," J. Phys. Chem. **97**, 8617 (1993).

[77]G. Hautier, A. Miglio, D. Waroquiers, G.-M. Rignanese, and X. Gonze, "How does chemistry influence electron effective mass in oxides? A high-throughput computational analysis," Chem. Mater. **26**, 5447 (2014).

[78]M. Gajdoš, K. Hummer, G. Kresse, J. Furthmüller, and F. Bechstedt, "Linear optical properties in the projector-augmented wave methodology," Phys. Rev. B **73**, 045112 (2006).

[79]G. Kresse, M. Marsman, and J. Furthmuller, "LOPTICS: frequency dependent dielectric matrix," VASP the Guide (University of Vienna, 2018).

[80]T. A. Stolyarova, E. A. Brichkina, A. V. Baranov, and E. G. Osadchii, "Enthalpy of formation of $Cu_2ZnSnSe_4$ from its constituent elements," Inorg. Mater. **55**, 755 (2019).

[81]T. A. Stolyarova, E. G. Osadchii, and A. V. Baranov, "Standard enthalpy of kesterite (Cu_2ZnSnS_4) formation," Geochem. Int. **57**, 109 (2019).

[82]L. C. Allen, "Electronegativity is the average one-electron energy of the valence-shell electrons in ground-state free atoms," J. Am. Chem. Soc. **111**, 9003 (1989).

[83]Y. Tian, B. Xu, and Z. Zhao, "Microscopic theory of hardness and design of novel superhard crystals," Int. J. Refract. Met. Hard Mater. **33**, 93 (2012).

[84]K. Gaal-Nagy and D. Strauch, "Ab-initio calculation of phonon dispersion curves: Accelerating q point convergence," Phys. Rev. B **77**, 024309 (2008).

[85]C. Gueymard, "The sun's total and spectral irradiance for solar energy applications and solar radiation models," Sol. Energy **76**, 423 (2004).

[86]M. A. Green and M. J. Keevers, "Optical properties of intrinsic silicon at 300 K," Prog. Photovoltaics: Res. Appl. **3**, 189 (1995).

[87]Ohio Supercomputer Center, Ohio Supercomputer Center (1987).